Computers, Materials & Continua

Tech Science Press

https://doi.org/10.32604/cmc.2026.076418

ARTICLE

# Physics-Informed Neural Networks for Bending Analysis of Graphene Origami-Enabled Auxetic Metamaterial Beams Based on Modified Coupled Stress Theory

**Zuoquan Zhu*, Menghan Wang, Xinyu Li and Mengxin Zhao**

School of Mathematics and Statistics, Zhengzhou Normal University, Zhengzhou, China

*Corresponding Author: Zuoquan Zhu. Email: zuoquanzhu@zznu.edu.cn

Received: 20 November 2025; Accepted: 20 January 2026; Published: 09 April 2026

**ABSTRACT:** Investigating the deformation behavior of graphene-reinforced composite structures holds significant engineering implications, while the rapid advancement of machine learning has introduced new technical approaches to structural bending analysis. In this study, we investigate the mechanical bending behavior of graphene origami (GOri)-enabled auxetic metamaterial beams using a physics-informed neural network (PINN). GOri-enabled auxetic metamaterials represent an innovative composite system characterized by a negative Poisson's ratio (NPR) and superior mechanical performance. Here, we propose a composite beam model incorporating the modified coupled stress theory (MCST) and employing the PINN method to solve higher-order bending governing equations. Compared to the analytical solution, the accuracy and effectiveness of the PINN framework as a meshless solver for higher-order partial differential equations are verified. The bending properties of metamaterial beams are studied by considering the mechanical properties and size effect of metamaterials. It was found that the length scale parameters, more graphene platelets, and a higher folding degree have the best reinforcement effect on composite beams. By systematically varying the GOri folding parameters and graphene content, we demonstrate the robustness of the PINN methodology in resolving microscale beam bending phenomena, particularly in capturing complex size-effect interactions.

**KEYWORDS:** Physics-informed neural networks; graphene origami; mechanical metamaterial; folding degrees; bending analysis

## 1 Introduction

In recent years, there has been growing interest in nanotechnology. Nanomaterials and nanostructures are used to manufacture micro-electromechanical and nanoelectromechanical systems, which are widely used in the fields of machinery, aerospace, electronics, and biomedical engineering. Micro-nano scale systems, including biosensors, electrochemical actuators, supercapacitors, nanotubes, and nanoprobes, predominantly use nanorods, nanobeams, nanoplates, and nanoshells as fundamental structural units [1–4]. Subsequently, advanced composites, such as functionally graded materials and graphene-based reinforced composites, have been developed, which have attracted scientists to establish mechanical models for their analysis. Among them, as a typical representative of the gradient structure, the mechanical behavior of mechanical metamaterial composite beams with a negative Poisson's ratio effect has attracted increasing attention from scholars.

Numerous experiments and theoretical studies have been conducted to effectively analyze and design metamaterial composite structures to characterize the mechanical behavior of the nanostructures.

Zhao et al. unveiled the mechanism of a highly tunable negative Poisson's ratio and developed micromechanical models based on genetic programming for the accelerated prediction of mechanical properties in GOri-based metallic metamaterials [5,6]. They then developed a model for the first time to study the bending [7], buckling, and postbuckling properties [8]. Their findings indicated that graphene origami can significantly influence the buckling and postbuckling behavior of metamaterial composite beams. Karami and Ghayesh [9] investigated the dynamics of auxetic metamaterials using various shear deformation theories. Ezzati et al. [10] and Ebrahimi and Ahari [11] investigated the free vibration behavior and vibration control of a graphene origami auxetic beam. Ebrahimi and Parsi [12] revealed the elastic wave characteristics of functionally graded graphene origami-reinforced metamaterial beams. Recently, several papers have been published on the thermal-mechanical coupling behavior of functionally graded graphene origami-enabled metamaterials [13]. On the other hand, certain experimental studies have proven the significance of the material microstructure and long-range interaction force on the mechanical response of micro-and nanostructured components [14–16]. Classical continuum theory cannot describe these small-scale effects well, but is widely used in macro-level structural modeling. Among the different modeling possibilities, one feasible method is to provide the so-called nonlocal continuum theory by directly modifying the classical theory. Over the years, researchers have proposed several non-local theories. The theories of stress gradient, strain gradient, and even integral type [17–20] provide some classic examples in which the small-scale effect is considered by introducing one or more internal length scale parameters. When structural dimensions are at the micrometer/nanometer scale, microscopic effects become particularly significant, especially for the study of size effects in graphene origami-enhanced microstructures.

In addition, advanced computational methods have significantly expanded the analytical capabilities of metamaterial composite systems. Neural networks, particularly deep-learning frameworks, have emerged as powerful tools in engineering disciplines such as materials science [21], solid mechanics [22], and fluid mechanics [23]. In the above research, the data-driven method was mainly used to minimize the error norm between network prediction and real data (training data) to train the model parameters [24]. However, their reliance on empirical correlations often limits their physical interpretability, and large-scale datasets are required for reliable predictions. To address these limitations, PINNs have gained traction by integrating governing differential equations into the learning process [25]. This framework introduces loss functions that enforce boundary conditions and conservation laws, thereby enabling the extraction of physics-compliant solutions without exhaustive data requirements. PINNs have been successfully applied to solve complex partial differential equations in fluid dynamics (e.g., Navier-Stokes equation [26]), phase transition phenomena (Cahn-Hilliard and Allen-Cahn equation [27]), and heat transfer processes [28]. In the field of solid mechanics, PINNs have demonstrated potential for modeling mechanical behaviors. For instance, Xue et al. [29] incorporated two loss functions, mass transfer and stress field, and used them to numerically obtain the solution of diffusion stress in an elastic sphere. Fallah and Aghdam [30] applied PINNs to study the bending and free vibration characteristics of three-dimensional functionally graded porous beams. Kianian et al. [31] extended the PINN approach to model the static bending response of micro/nanoelectromechanical systems. Moreover, Bazmara et al. [32] proposed an NN framework based on physical information to predict the nonlinear buckling behavior of 3D functionally graded (FG) porous beams on elastic foundations. These studies highlight PINN's ability to handle higher-order differential equations and achieve close agreement with the numerical solutions. However, PINN is rarely used to solve the mechanical behavior of graphene origami composite beams, considering the size effect.

The key contributions of this work are as follows: On the one hand, a large body of scholarly work has employed PINN to investigate the bending behavior of functionally graded material (FGM) nanobeams and nanoplates. These studies typically rely on small-scale theories, such as the strain gradient theory

and nonlocal elasticity theory, yet their research focus remains confined to traditional functionally graded materials rather than mechanical metamaterials. However, some scholars have applied PINN to analyze the bending or buckling responses [33] of origami metamaterial composite beams/plates; the critical factor of the size effect has been overlooked in their investigations. Against this backdrop, this study addresses the bending problem of beams subjected to the combined influence of the size effect and metamaterial characteristics. Since the differential equations incorporate physical information, only the loss associated with boundary conditions needs to be considered during model training, eliminating the need for mesh partitioning and effectively improving computational efficiency. By employing both numerical methods and mesh-free PINN methods for parallel solution, this study aims to contribute to the advancement of research in this field.

In this study, a physics-informed neural network was used to analyze the bending behavior of graphene origami-reinforced metamaterial beams. The governing equation, a fourth-order differential equation with variable coefficients, was combined with the boundary conditions formulated using Hamilton's principle. A deep feedforward neural network is constructed to approximate the beam bending deflection. Its parameters are optimized by minimizing a composite loss function that forces both the governing equations and boundary constraints. To validate the proposed approach, PINN predictions were compared against available analytical solutions. The convergence and accuracy of the PINN in predicting deflections under different boundary conditions were studied. Then, the influence of the graphene origami content, distribution, and size parameter on the deflection of graphene origami-reinforced metamaterial beams is investigated.

## 2 Mathematical Formulations

### *2.1 Effective Material Properties*

Consider a functionally graded graphene origami/Sn (GOri/Sn) composite microbeam with a rectangular cross-section. The microbeam had a length $L$, height $h$, and width $b$, as schematically depicted in Fig. 1. The rectangular Cartesian coordinate axes used to study infinitesimal bending deformations are also shown in the figure. Here, the neutral surface of the beam lies in the x-y plane, and the positive $z$-axis points upward along the thickness direction. The beam material was assumed isotropic and linearly elastic. Moreover, this study extends the application of the machine-learning-based method to the bending analysis of microbeams using PINN.

The elastic modulus ($E_e$), Poisson's ratio ($\nu_e$), and density ($\rho_e$) of the materials were determined using a micromechanical model assisted by genetic programming (GP), as proposed by Zhao et al. [5,6]

$$\begin{aligned} E_e &= \frac{1+\xi\eta V_{GR}}{1-\eta V_{GR}} E_{Sn} \times f_E\left(H_{GR}, V_{GR}, T\right) \\ \nu_e &= \left(\nu_{GR} V_{GR} + \nu_{Sn} V_{Sn}\right) \times f_\nu\left(H_{GR}, V_{GR}, T\right) \\ \rho_e &= \left(\rho_{GR} V_{GR} + \rho_{Sn} V_{Sn}\right) \times f_\rho\left(V_{GR}, T\right) \end{aligned} \tag{1}$$

The coefficients for material ($\eta$) and size ($\xi$) are outlined below:

$$\eta = \frac{\left(E_{GR}/E_{Sn}\right)-1}{\left(E_{GR}/E_{Sn}\right)+\xi}, \xi = 2\left(l_{GR}/t_{GR}\right) \tag{2}$$

where $l_{GR}$ and $t_{GR}$ denote the length and thickness of the graphene, respectively. The transformation functions, $f_E\left(H_{GR}, V_{GR}, T\right)$ ,$f_\nu\left(H_{GR}, V_{GR}, T\right)$ and $f_\rho\left(V_{GR}, T\right)$were derived using the GP algorithm developed by Zhao et al. [5,6]

$$f_E\left(H_{GR}, V_{GR}, T\right) = 1.11 - 1.22V_{GR} - 0.134\left(\frac{T}{T_0}\right) + 0.559V_{GR}\left(\frac{T}{T_0}\right) - 5.5H_{GR}V_{GR} + 38H_{GR}V_{GR}^2 - 20.6H_{GR}^2V_{GR}^2 \tag{3a}$$

$$f_v\left(H_{GR}, V_{GR}, T\right) = 1.01 - 1.43V_{GR} + 0.165\left(\frac{T}{T_0}\right) - 16.8H_{GR}V_{GR} - 1.1H_{GR}V_{GR}\left(\frac{T}{T_0}\right) + 16H_{GR}^2V_{GR}^2 \tag{3b}$$

$$f_\rho\left(V_{GR}, T\right) = 1.01 - 2.01V_{GR}^2 - 0.0131\left(\frac{T}{T_0}\right) \tag{3c}$$

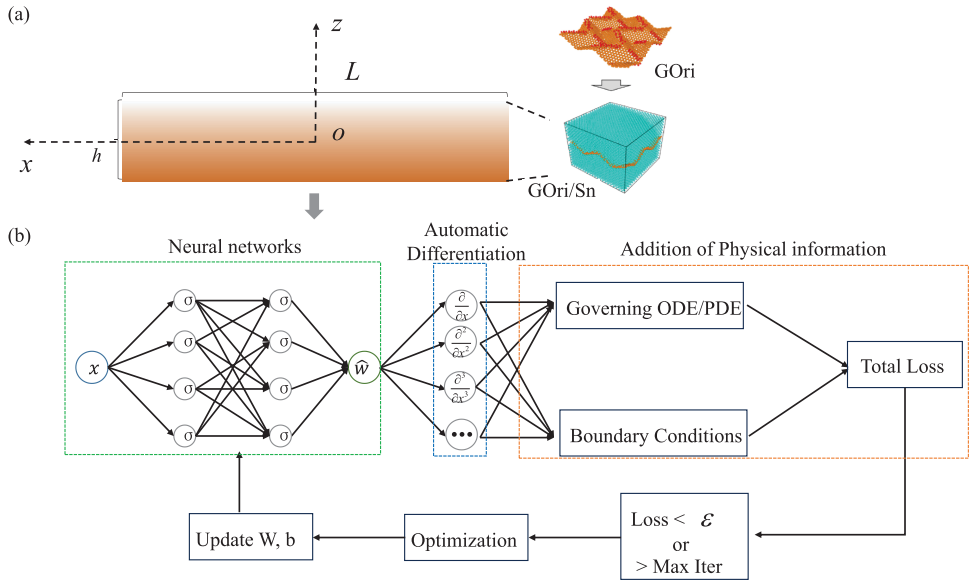


**Figure 1:** (**a**) The geometry and cross-section of the GOri/Sn composite beam. (**b**) Schematic of PINN framework for beam bending analysis.

With the temperature $T_0$ set at 300 K, the current ambient temperature can be confidently represented as $T$. Because the influence of temperature was not considered in this study, we assumed that the temperature remained $T = T_0$. The volume fractions $V_{GR}(k)$ of the $k$th layer for two graphene content distribution are considered. On one hand, the surface layers are GOri rich while the middle layer is poor in the $X - W_{GR}$ beam, $V_{GR}(k) = 2V_{GR}\left|2k - N_L - 1\right|/N_L$ in which $k = 1, 2, \cdots, N_L$ ($N_L$: total layer number) [34–36]. On the other hand, the GOri content is the same in each layer in a $U - W_{GR}$ beam, $V_{GR}(k) = V_{GR}$.

At the same time, the H coverage $H_{GR}(z)$ with uniform distribution $U - H_{GR}$ and non-uniform distribution $X - H_{GR}$ along the thickness direction is governed by

$$U - H_{GR} : H_{GR}(z) = H_{GR} \tag{4a}$$

$$X - H_{GR} : H_{GR}(z) = H_{GR}\cos\left(z\pi/h\right) \tag{4b}$$

Taking the four distribution scenarios as an example, the effective Poisson's ratio $v_e$ of the GOri/Sn composite beam, as a function of the GOri parameter model, is graphically presented in Fig. 2. Fig. 2 depicts the effective Poisson's ratio distribution of the graphene origami-reinforced composite beams along the thickness direction. With an increase in the GOri content and folding degree, the GOri/Sn composite beam shows an auxetic effect (i.e., the Poisson's ratio is less than zero). In the subsequent discussion, we explore the bending behavior of composite beams with auxetic effects caused by the graphene origami content and

folding degree. In addition, a similar phenomenon of graphene origami composite structure patterns with different layers and non-uniform distribution can be found in [34,35].

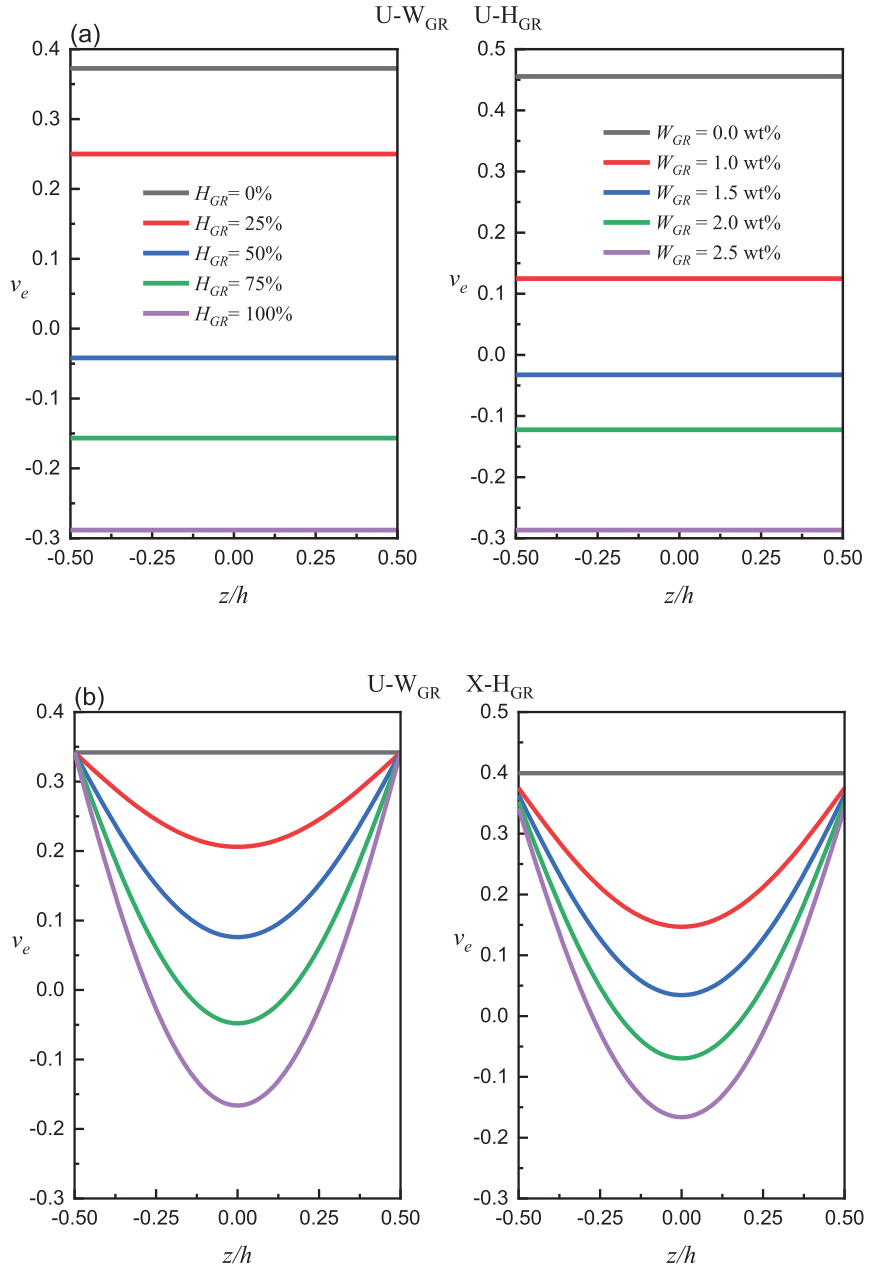


**Figure 2:** (Continued)

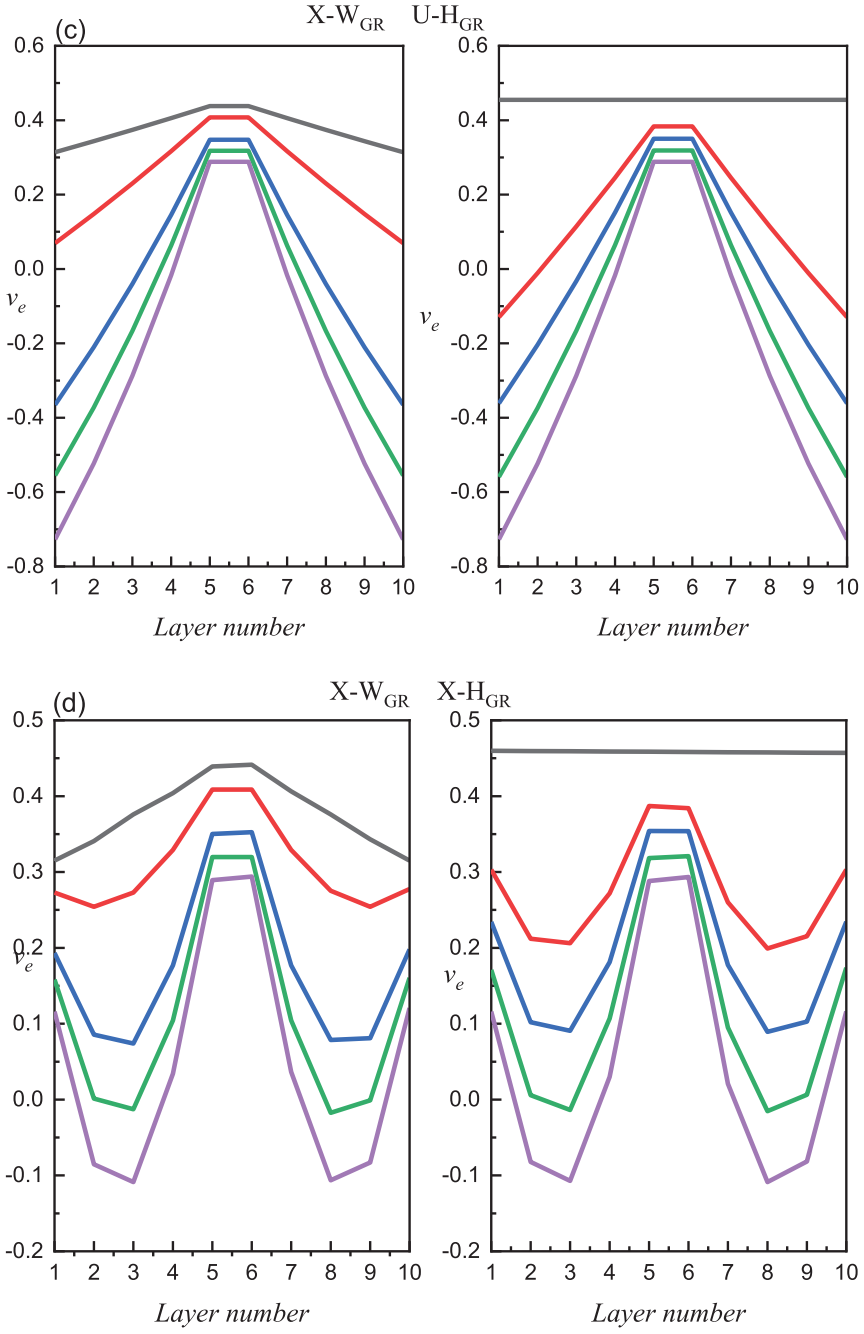


**Figure 2:** The variation of Poisson's ratio for GOri/Sn composite beam for different composite patterns: (**a**) $U-W_{GR}, U-H_{GR}$; (**b**) $U-W_{GR}, X-H_{GR}$; (**c**) $X-W_{GR}, U-H_{GR}$; (**d**) $X-W_{GR}, X-H_{GR}$.

### *2.2 Modified Couple Stress Theory*

Based on the modified coupled stress theory [37], the strain energy $U$ of an isotropic elastic material in the domain $\Omega$ can be formulated as follows

$$U = \frac{1}{2}\int_{\Omega} (\boldsymbol{\sigma}:\boldsymbol{\varepsilon} + \mathbf{m}:\boldsymbol{\chi})\, \mathrm{d}\Omega \tag{5}$$

where $\boldsymbol{\sigma}$, $\boldsymbol{\varepsilon}$, $\mathbf{m}$, and $\boldsymbol{\chi}$ represent the Cauchy stress tensor, strain tensor, deviatoric part of the couple stress tensor, and symmetric curvature tensor, respectively. The tensors are defined as follows:

$$\boldsymbol{\sigma} = \lambda tr\left(\boldsymbol{\varepsilon}\right)\mathbf{I} + 2\mu\boldsymbol{\varepsilon}, \boldsymbol{\varepsilon} = \frac{1}{2}\left[\nabla\mathbf{u} + \left(\nabla\mathbf{u}\right)^{T}\right] \tag{6}$$

$$\mathbf{m} = 2\mu\ell^{2}\chi, \chi = \frac{1}{2}\left[\nabla\theta + \left(\nabla\theta\right)^{T}\right] \tag{7}$$

where $\mathbf{u}$ denotes the displacement vector, $\theta = \text{curl}\left(\mathbf{u}\right)/2$ represents the rotation vector, $\ell$ is the material length scale parameter introduced to account for the size effect, and $\lambda$ and $\mu$ are Lamé constants in classical continuum mechanics. Note that $\mu$ is also known as shear modulus. They can be written as

$$\lambda = \frac{E_e \nu_e}{\left(1+\nu_e\right)\left(1-2\nu_e\right)} \tag{8}$$

$$\mu = \frac{E_e}{2\left(1+\nu_e\right)} \tag{9}$$

### *2.3 Governing Equations*

In this study, the Euler-Bernoulli beam theory was utilized to model the beam. Consequently, the displacement field can be expressed as

$$u_1\left(x,z\right) = -z\frac{\partial w}{\partial x} \tag{10}$$

$$u_2\left(x,z\right) = 0 \tag{11}$$

$$u_3\left(x,z\right) = w\left(x\right) \tag{12}$$

where $w\left(x\right)$ represents the transverse displacements on the midplane of the FG nanobeam.

The tensors associated with Eqs. (6) and (7) can be written as

$$\varepsilon_{xx} = -z\frac{\partial^2 w}{\partial x^2}, \theta_y = -\left(\frac{\partial w}{\partial x}\right), \chi_{xy} = -\frac{1}{2}\left(\frac{\partial^2 w}{\partial x^2}\right) \tag{13}$$

Substituting Eq. (13) into Eq. (6), the strain energy $U$ can be written as:

$$U = \frac{1}{2}\iint_V \int \left[\varepsilon_{xx}\sigma_{xx} + 2m_{xy}\chi_{xy}\right]dv + \frac{1}{2}\iiint_V \int \left[\sigma_{xx}\left(-z\frac{\partial^2 w}{\partial x^2}\right) + 4\ell^2\mu\chi_{xy}^2\right]dv \tag{14}$$

By employing the stress tensor from Eq. (6) and taking the variation in the strain energy, we obtain

$$\begin{aligned}
\delta U &= \frac{1}{2}\iint_V \int \delta\left[\left(\lambda+2\mu\right)\left(-z\frac{\partial^2 w}{\partial x^2}\right)^2 + \ell^2\mu\left(\frac{\partial^2 w}{\partial x^2}\right)^2\right]dv \\
&= \frac{1}{2}\int_0^L \int_A \left[\left(\lambda+2\mu\right)\delta\left(-z\frac{\partial^2 w}{\partial x^2}\right)^2 + \ell^2\mu\delta\left(\frac{\partial^2 w}{\partial x^2}\right)^2\right]dAdx \\
&= \int_0^L \int_A \left[\left(\lambda+2\mu\right)z^2\frac{\partial^4 w}{\partial x^4}\delta w + \ell^2\mu\frac{\partial^4 w}{\partial x^4}\right]dAdx \\
&= \int_A \left[A_{11}\frac{\partial^4 w}{\partial x^4}\delta w + \ell^2 B_{11}\frac{\partial^4 w}{\partial x^4}\delta w\right]dx
\end{aligned} \tag{15}$$

in which $A_{11} = \int_A (\lambda + 2\mu) z^2 dA$ and $B_{11} = \int_A \mu dA$.

By disregarding the body force and body couple, the work $W$ performed by external forces in the form of transverse loading $q(x)$ can be written as

$$W = \int_{x=0}^{L} q(x) w(x) \, \mathrm{d}x \tag{16}$$

Substitute Eqs. (13) and (15) into Hamilton's principle and setting the resulting expression to zero, that is,

$$\delta \Pi = \int_0^L (\delta U - \delta W) \, \mathrm{d}x = 0 \tag{17}$$

The governing equations of motion can be derived as [38]

$$A_{11} \frac{\partial^4 w}{\partial x^4} + \ell^2 B_{11} \frac{\partial^4 w}{\partial x^4} = q(x) \tag{18}$$

In addition, we can define the equivalent stiffness as $D_e = D + D^\ell = A_{11} + \ell^2 B_{11}$. It can be observed that for $D^\ell = \ell = 0$, Eq. (18) yields the governing equation of classical beam theory. Based on our knowledge of material mechanics, it is easy to obtain analytical expressions for the deflection of a microbeam under different boundary conditions with finite element method.

## 3 Physics-Informed Neural Networks Framework

This section employs a general PINN model to solve the bending Eq. (18). PINNs, a specialized class of artificial neural networks, are used to obtain an approximate solution of the governing differential equations. To solve Eq. (18), a neural network is constructed with the spatial variable $x$ as its input to approximate the solution. Within the PINN framework, a feedforward neural network (FNN) [39] is commonly adopted as the neural network architecture [40,41] due to its strong function approximation capability and structural simplicity. An illustration of the FNN is shown in Fig. 1. Thus, the approximate solution can be written as

$$\hat{w}(x) = F(x) = \mathrm{N}^L(x; W, b) \tag{19}$$

where $\hat{w}(x)$ is the approximate solution, $F(x)$ denotes the FNN. The FNN is structured as an $L$-layer deep neural network. It accepts an input vector $x$, produces an output vector $\hat{w}$, and is parameterized by a weight matrix $W$ and a bias vector $b$. The network was trained using a backpropagation algorithm [42], which iteratively reduces a composite loss function. This loss function quantifies the discrepancy between the network's predictions and the target solution [43]. In the context of PINNs, the loss function incorporates differential equations and boundary conditions

$$Loss = L_{PDE} + L_{BC} \tag{20}$$

where $L_{PDE}$ and $L_{BC}$ represent the losses associated with partial differential equations and boundary conditions, respectively. It is noteworthy that the partial differential term within the loss function can be analytically derived using automatic differentiation [44].

The loss function endowed with physical constraints is a crucial element in PINNs. It facilitates the training of neural networks in accordance with the physical laws. Within the current PINN-based computational mechanics framework, two main types of loss functions are commonly employed: the allocation loss function and the energy-based loss function. In the allocation loss function, the residuals

of the equilibrium equation and boundary conditions were compelled to be zero at each sample point. In this study, an allocation loss function was adopted to formulate the loss function. In this approach, the mean-square error is used to define the loss function:

$$Loss = \frac{1}{n}\sum_{i=1}^{n} R_{PDE}^{2}\left(x_i\right) + \frac{1}{m}\sum_{i=1}^{m} R_{BC}^{2}\left(x_i\right) = \frac{1}{n}\sum_{i=1}^{n}\left[D_e \frac{\partial \hat{w}\left(x_i\right)}{\partial x^4} - q\left(x_i\right)\right]^2 + \left(\hat{w}\left(0\right)\right)^2 + \left(\hat{w}\left(L\right)\right)^2 + \left(\frac{\partial^2 \hat{w}\left(0\right)}{\partial x^2}\right)^2 + \left(\frac{\partial^2 \hat{w}\left(L\right)}{\partial x^2}\right)^2 \tag{21}$$

where $R_{PDE}$ and $R_{BC}$ are the residuals of the equilibrium equation and the boundary conditions, respectively. Here, $n$ represents the total number of sample points and $m$ is the number of sample points on the boundary. Subsequently, the training algorithm is implemented to search for the neural network mapping that satisfies the governing equations at sample points. A schematic of the PINN algorithm applied to the bending equation is illustrated in Fig. 1b.

## 4 Results and Discussion

The developed physics-informed neural network was used for numerical calculations. In addition, to verify the reliability of the PINN approximate solution, the numerical results obtained based on finite element and analytical expressions are also presented and used as reference numerical solutions, in which the focus of the analysis is on the bending behavior of GOri/Sn metamaterial microbeams. In this study, all tasks were trained using an NVIDIA Titan RTX GPU. As depicted in Fig. S1 (Supporting Information), we trained three different neural network architectures with varying numbers of hidden layers. Based on the training speed, convergence curve volatility, and forecasting performance of each neural network, we selected a three-layer network with 40 nodes as the architecture for this study. As shown by the error curve in Fig. S2 (Supporting Information), compared to other adaptive stochastic gradient descent methods such as stochastic gradient descent (SGD) and root mean square propagation (RMSPro), the Adam algorithm demonstrates superior performance in model optimization. It enables faster computation and convergence, making it an ideal optimization algorithm for neural network training. Additionally, the Adam optimization scheme [45] is prominent, extensively applied, and highly adaptable within the PINN methodology. In this study, an Adam optimizer with an initial learning rate of $10^{-4}$ is used to train the deep neural network (DNN). Fig. S3 (Supporting Information) shows the variation in loss function values during model training under different activation functions. When using rectified linear unit (ReLU) as the activation function, the loss decreases more slowly, ultimately leading to underfitting in the final training results. When training models with tanh and Sigmoid as activation functions, the loss function converges more rapidly. Furthermore, upon convergence, the loss value of the tanh model is lower than that of the Sigmoid model. Thus, the hyperbolic tangent (tanh) function was used as the activation function within the FNNs [46]. In the workflow described in this paper, 200 sample points within the domain and 100 boundary sample points were generated using the Latin hypercube sampling (LHS) method. The maximum training iterations were set to 50,000, and parameters were initialized using the Glorot normal distribution initializer. Geometric parameters of pristine graphene: $l_{Gr}$ = 83.76Å and $t_{Gr}$ = 3.4 Å [5]. The material parameters at room temperature are presented in Table 1.

**Table 1:** Mechanical properties of graphene and Sn.

| | Sn matrix [47] | Graphene [5] |
|---|---|---|
| Young's modulus (GPa) | 51 | 929.57 |
| Mass density (kg/m$^3$) | 8800 | 1800 |
| Poisson's ratio | 0.34 | 0.22 |

### *4.1 Validation*

To check the accuracy of the numerical calculation results of the analytical method, considering the thickness of the homogeneous microbeam $h = 1\,\mu m$ and ignoring the influence of origami graphene, the approximate solution of PINN in this study was compared with the analytical solution of deflection under three boundary conditions, as shown in Fig. 3. We adopted the finite element method to obtain its analytical solution, the details of which are as follows: (1) Mesh size and type: The computational domain was discretized using 4-node quadrilateral elements with a mesh density of 0.1 nm element size to balance accuracy and computational efficiency. Mesh convergence tests were performed to confirm that further refinement did not alter the results significantly. (2) Solver specifications: The finite element method (FEM) simulations were conducted using COMSOL Multiphysics 6.3, with a direct solver for these cases and a convergence tolerance of $1 \times 10^{-6}$ for displacement residuals and $1 \times 10^{-6}$ for force residuals (Fig. S4, Supporting Information). (3) Boundary conditions: The same boundary conditions as those applied in the PINN model were enforced in the FEM, including uniform load $q$ on the surface of the beam and the displacement boundary condition. To facilitate the comparison and discussion of the calculation results, the dimensionless deflection is defined as $\overline{w} = w\left(\frac{EI}{qL^4}\right)$.

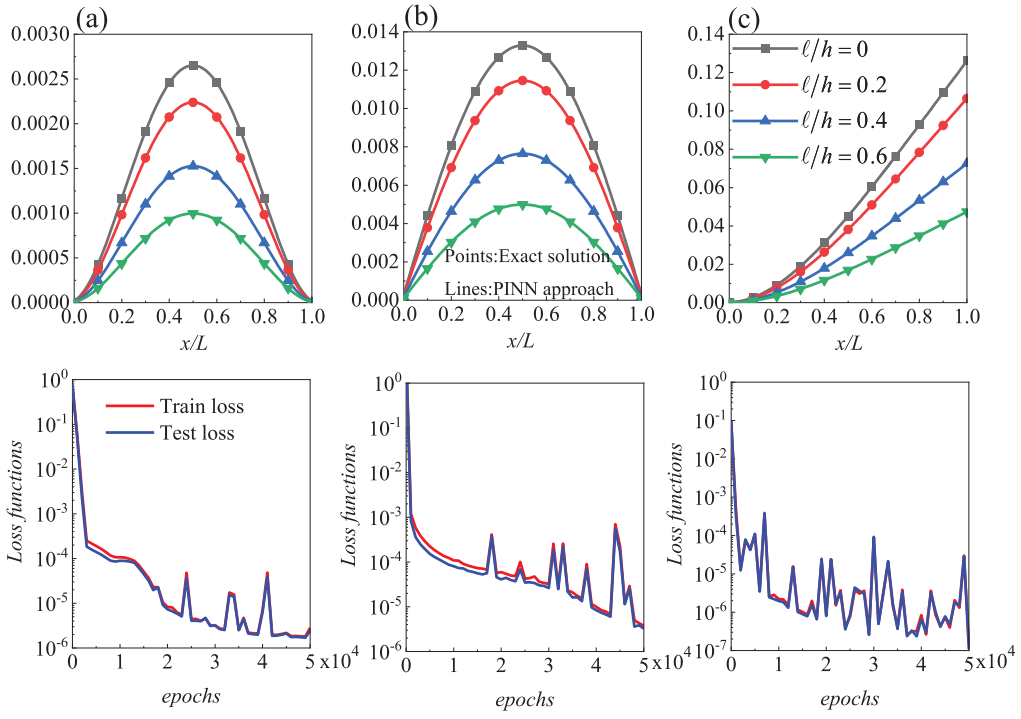


**Figure 3:** Non-dimensional deflection of micro-beam and loss function value of (**a**) C-C, (**b**) S-S and (**c**) C-F beams under uniform distributed load ($L/h = 10$, $q = 1N/m$, $\ell/h = 0, 0.2, 0.4, 0.6$).

Fig. 3 shows the nondimensional deflection of a homogeneous microbeam with three boundary conditions: simply supported at both ends, fixed at both ends, and a cantilever beam, along with the values of the loss function. The PINN prediction under the three boundary conditions is consistent with the exact solution. In addition, after 10,000 iterations, the loss function values in all three cases quickly decreased to less than $10^{-4}$. This indicates that the network converged to the final solution with a high degree of accuracy.

To investigate the validity of the developed PINN approach, the present results are compared with those obtained by Park and Gao [48] based on the couple stress theory shown in Fig. 4. The figure clearly demonstrates excellent agreement between the results derived from the PINN approach and those reported in the literature.

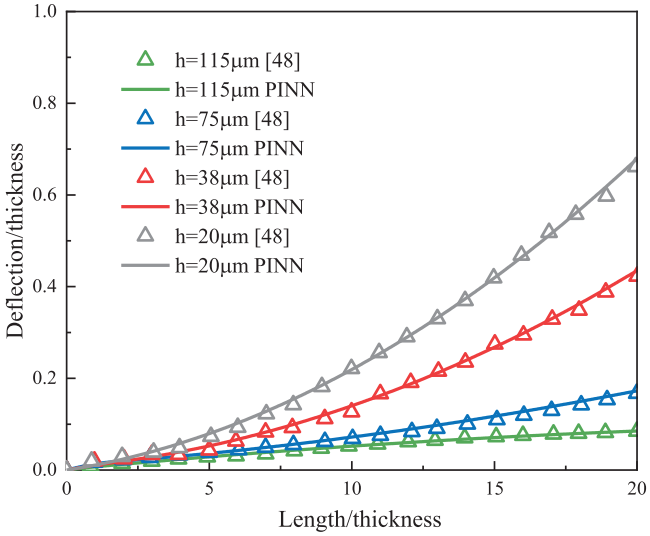


**Figure 4:** Comparing the present results with the work of Park and Gao [48] in variation of dimensionless deflection of beam under C–F boundary conditions with changes in beam thickness.

### *4.2 Parametric Analysis*

A comprehensive parameter analysis was carried out through parameter research based on the PINN approach. The bending characteristics of composite beams with different porosities, slenderness ratios, and boundary conditions were studied.

To provide further insight into the outputs of the PINN approach, Fig. 5 describes how the maximum deflection of the graphene origami composite beam is affected by the scale parameters, graphene origami content, and folding degree (at this time, the folding degree of graphene is 50%) under a uniformly distributed load and fixed boundary at both ends. It can be observed that the dimensionless maximum deflection decreased with increasing graphene content. This is because when the graphene content increased, the equivalent stiffness of the GOri/Sn composites increased, and they exhibited better bending performance. However, with an increase in the folding degree of graphene (the mass fraction of graphene is 2.5 wt%), the equivalent elastic modulus of the composite beam decreases and exhibits the characteristics of metamaterials [49,50], and it is observed that the maximum deflection increases slightly. Considering the size effect, the increase in graphene content reduced the maximum deflection by 61.5% ($\ell/h$ = 0), and the maximum deflection increased by 16.7% ($\ell/h$ = 0). This is due to the fact that the stiffness-hardening effect in microscale by the MCST. Due to the competing mechanisms between the stiffness hardening effect of the size effect

and the stiffness weakening caused by graphene folding, the deflection trend gradually flattens as the folding degree increases.

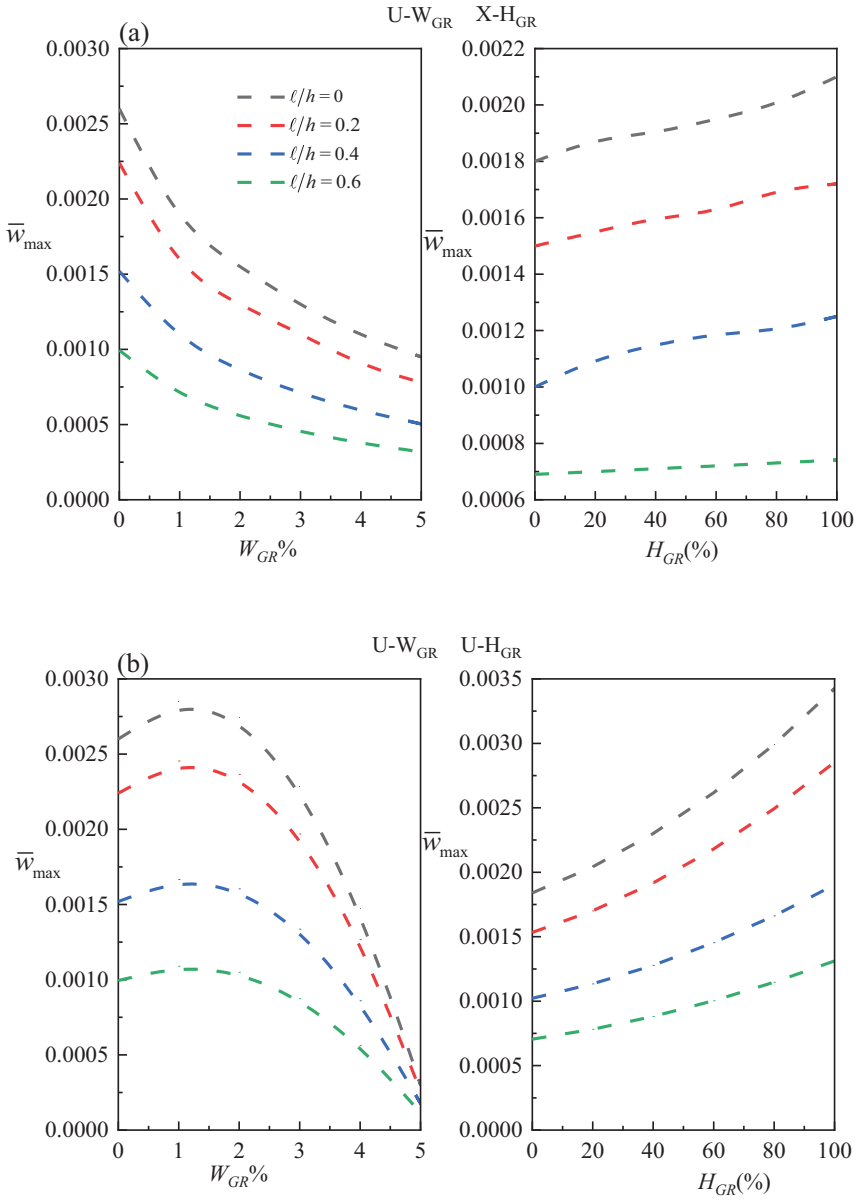


**Figure 5:** (Continued)

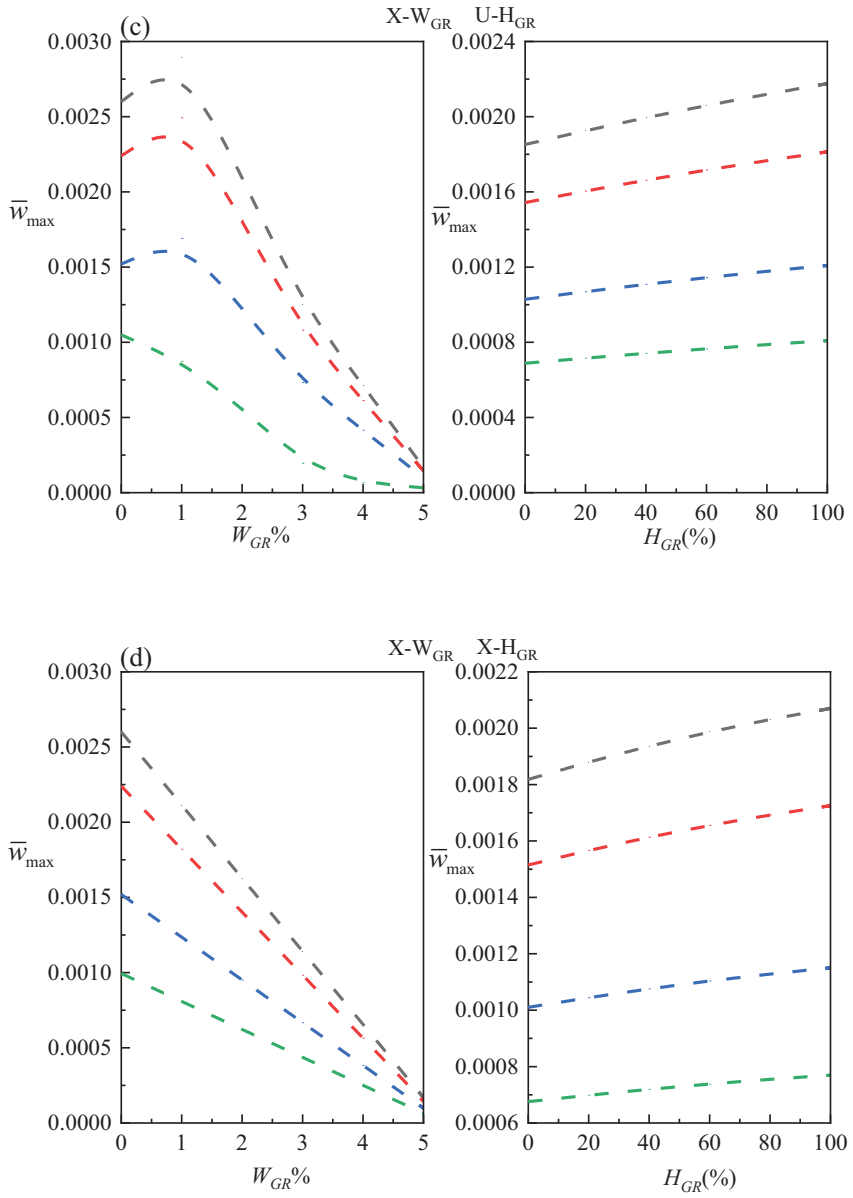


**Figure 5:** Dimensionless maximum deflection with C-C boundary conditions vs. GOri content and folding degree for different composite patterns (**a**) $U - W_{GR}, X - H_{GR}$; (**b**) $U - W_{GR}, U - H_{GR}$; (**c**) $X - W_{GR}, U - H_{GR}$; (**d**) $X - W_{GR}, X - H_{GR}$.

Fig. 6 shows the influence of the scale parameters, graphene origami content, and folding degree on the maximum deflection of the graphene origami composite beam under a uniformly distributed load and simply supported boundary conditions at both ends (at this time, the folding degree of graphene is 50%), and a conclusion similar to that in Fig. 5 can be obtained. Increasing the graphene origami content enhances the effective stiffness, while increasing the folding degree reduces the effective stiffness of the composite beam. In addition, considering the size effect, an increase in graphene content will lead to a maximum deflection reduction of 64.3% ($\ell/h = 0$), and the maximum deflection of graphene folding will increase by 27.5% ($\ell/h = 0$). The primary cause of this change stems from the stiffness hardening effect from the size effect.

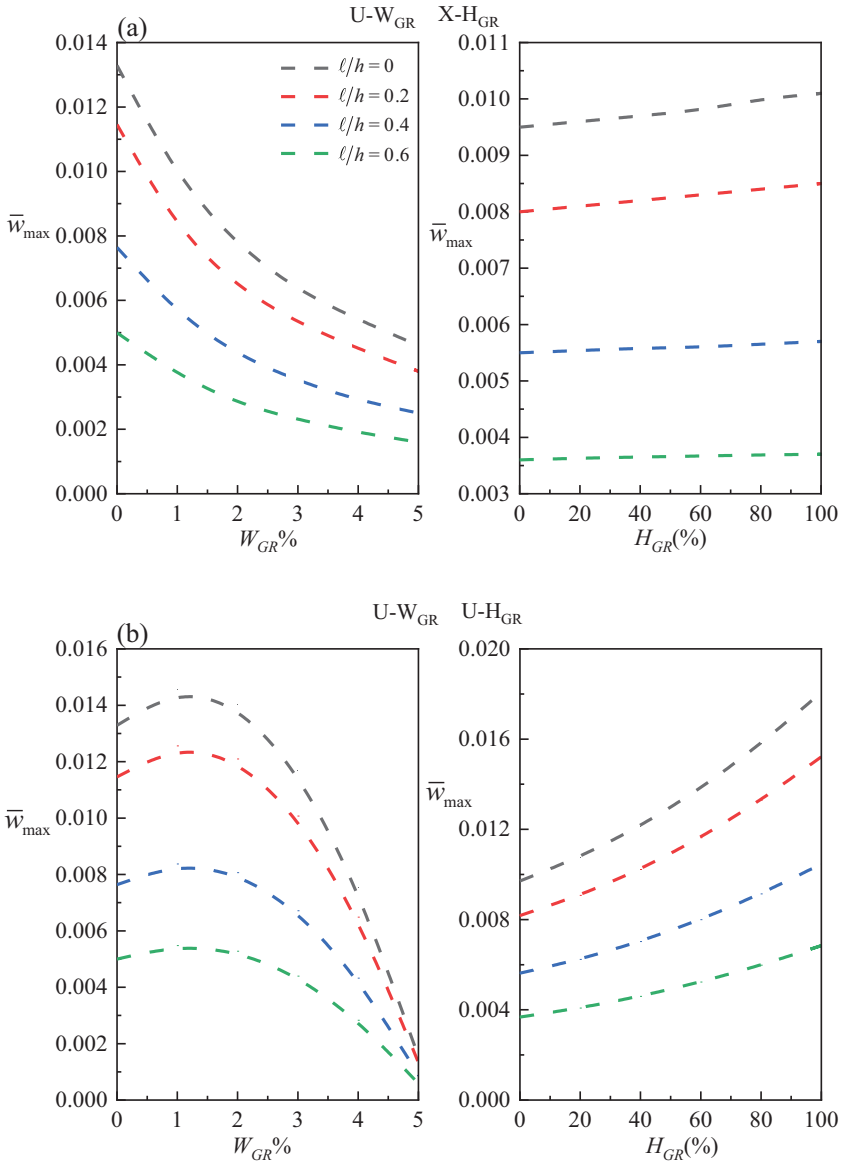


**Figure 6:** (Continued)

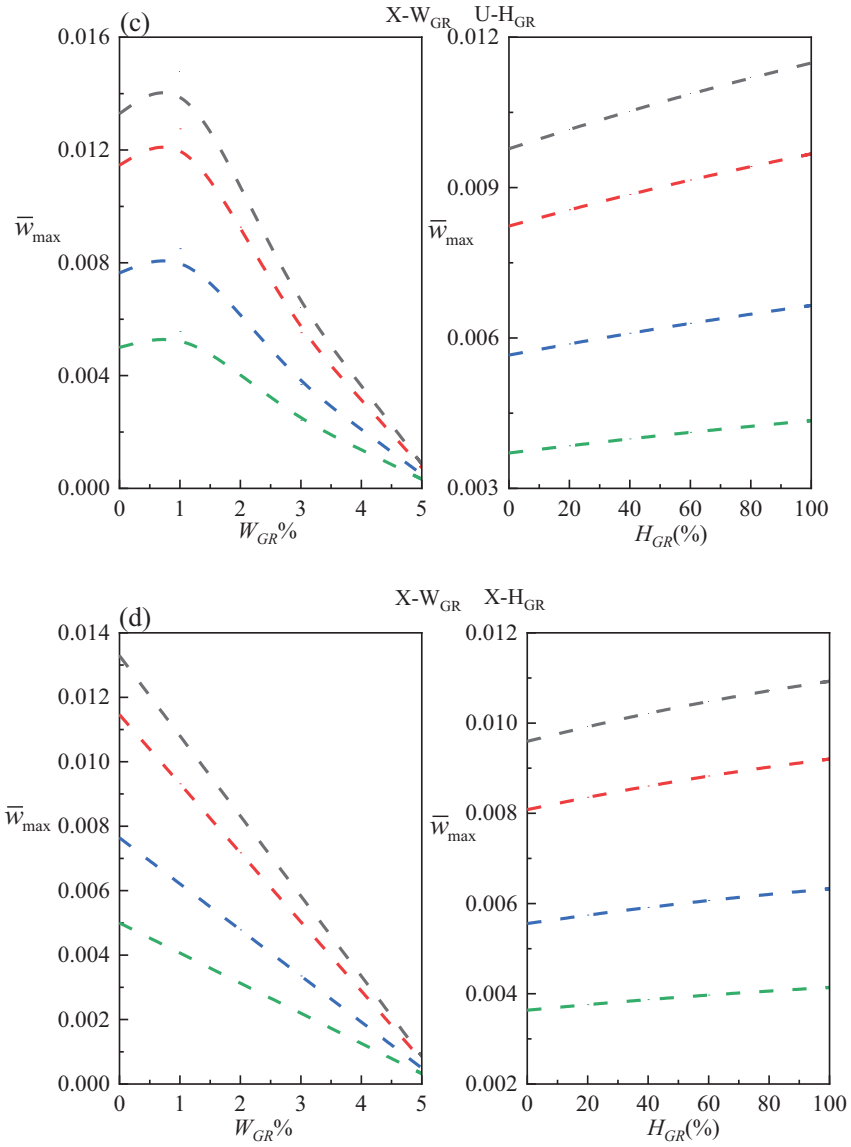


**Figure 6:** Dimensionless maximum deflection with S-S boundary conditions vs. GOri content and folding degree for different composite patterns (**a**) $U - W_{GR}, X - H_{GR}$; (**b**) $U - W_{GR}, U - H_{GR}$; (**c**) $X - W_{GR}, U - H_{GR}$; (**d**) $X - W_{GR}, X - H_{GR}$.

Fig. 7 describes the influence of scale parameters, graphene origami content, and folding degree on the maximum deflection of the graphene origami composite beam under the condition of C-F boundary conditions. We observe that an increase in graphene content leads to an increase in effective stiffness, thereby reducing the maximum bending deflection. Simultaneously, the degree of graphene folding weakens the bending performance. Based on the MCST, the maximum deflection decreases by 60% ($\ell/h = 0$) with increased graphene content. In contrast, it increases by 8.2% ($\ell/h = 0$) due to the folding degree of graphene origami.

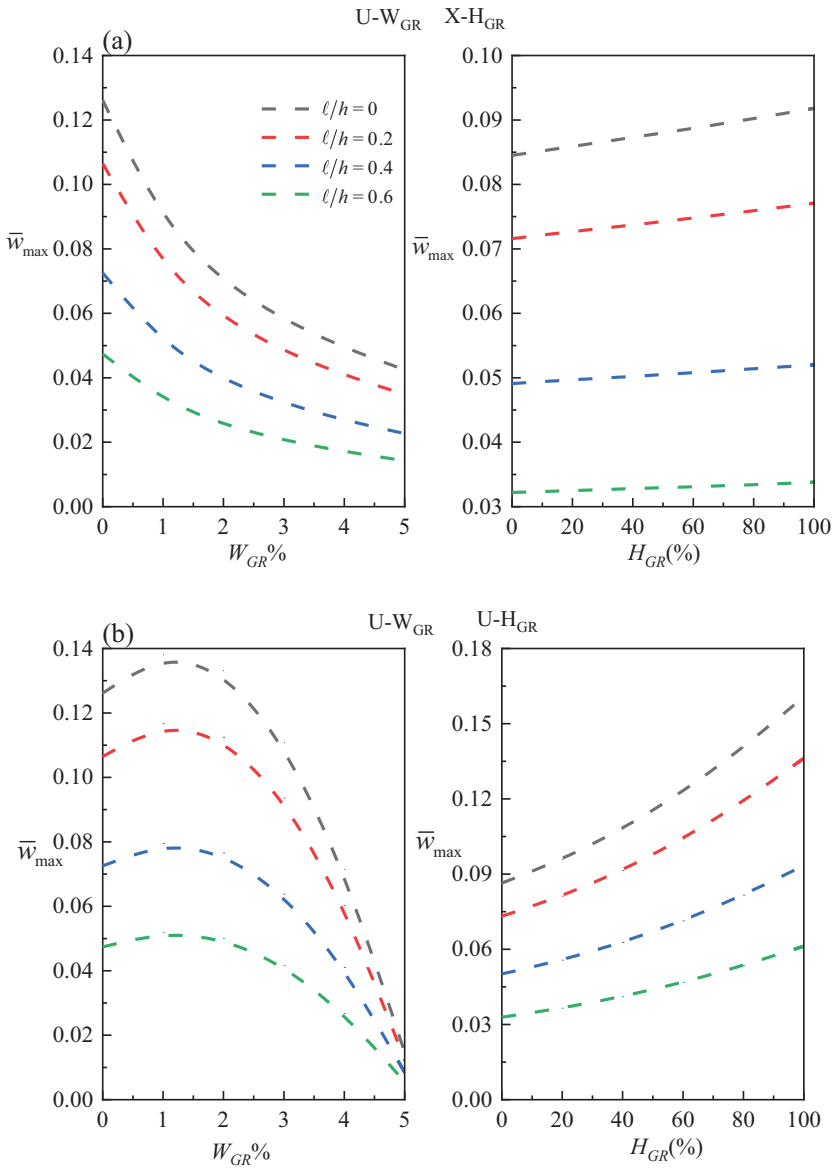


**Figure 7:** (Continued)

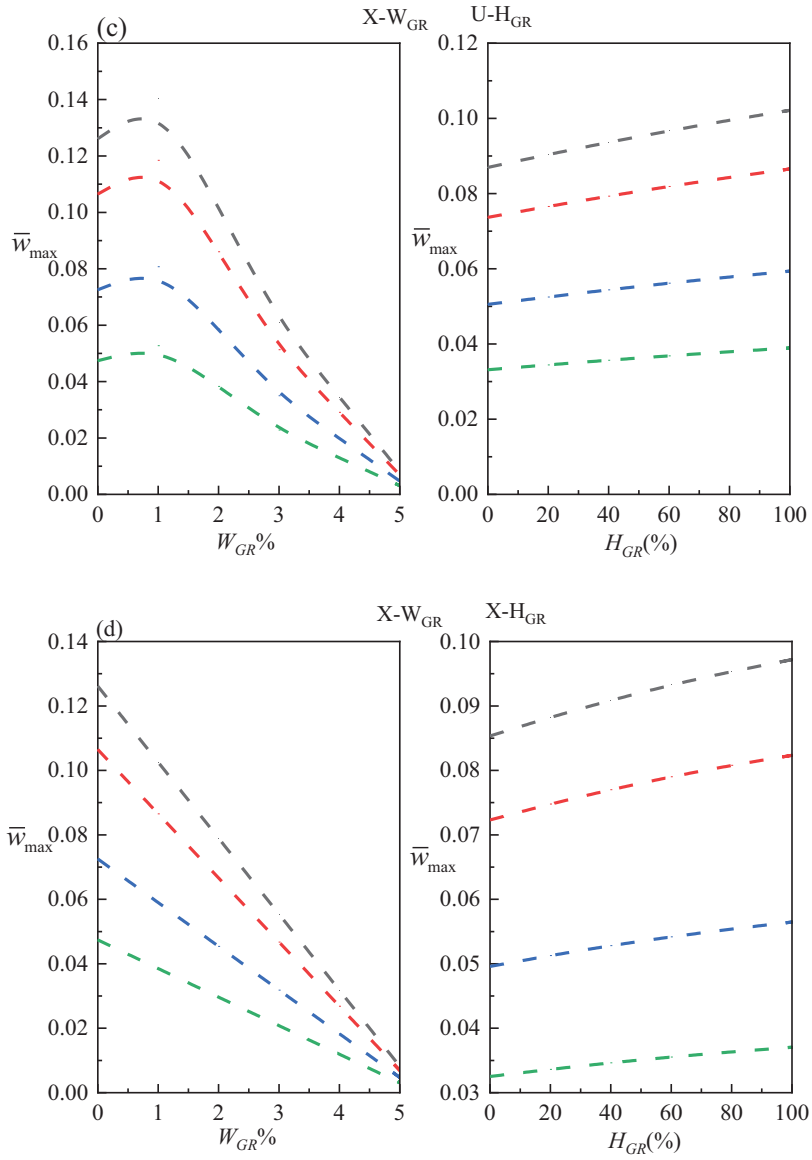


**Figure 7:** Dimensionless maximum deflection with C-F boundary conditions vs. GOri content and folding degree for different composite patterns (**a**) $U-W_{GR}, X-H_{GR}$; (**b**) $U-W_{GR}, U-H_{GR}$; (**c**) $X-W_{GR}, U-H_{GR}$; (**d**) $X-W_{GR}, X-H_{GR}$.

From Figs. 5–7, we can obtain the following results regarding the pattern distribution under three boundary conditions. In the H coverage with an X-type distribution, increasing the GOri content reduces the dimensionless deflection. In contrast, for H coverage with a U-type distribution, increasing the GOri content causes the dimensionless deflection to first increase and then decrease. Additionally, as shown in the Figs. 5 and 7, with an increase in the graphene folding degree, the dimensionless maximum bending deflection occurs, which is attributed to the reduction in Young's modulus and the emergence of a negative Poisson's ratio. Furthermore, the results indicate that among the tested configurations, the $X-W_{GR}, X-H_{GR}$ beam demonstrates the smallest dimensionless maximum bending deflection, followed in sequence by the $X-W_{GR}, U-H_{GR}$ beam, $U-W_{GR}, X-H_{GR}$ beam, and $U-W_{GR}, U-H_{GR}$ beams.

These findings suggest that dispersing a higher GOri content near the beam surfaces can enhance the structural performance of the metamaterial.

Finally, to further reveal the mechanism of graphene origami, we determined the influence of the slenderness ratio on the static bending behavior of graphene origami metamaterial and homogeneous beams, as shown in Fig. 8. In this case, we do not consider the size effect. As expected, increasing the slenderness ratio led to greater bending deformation. When the composite beam is made of metamaterials, compared to the pure Sn beam, a smaller deflection can be obtained; that is, the stability of the metamaterial beam is better.

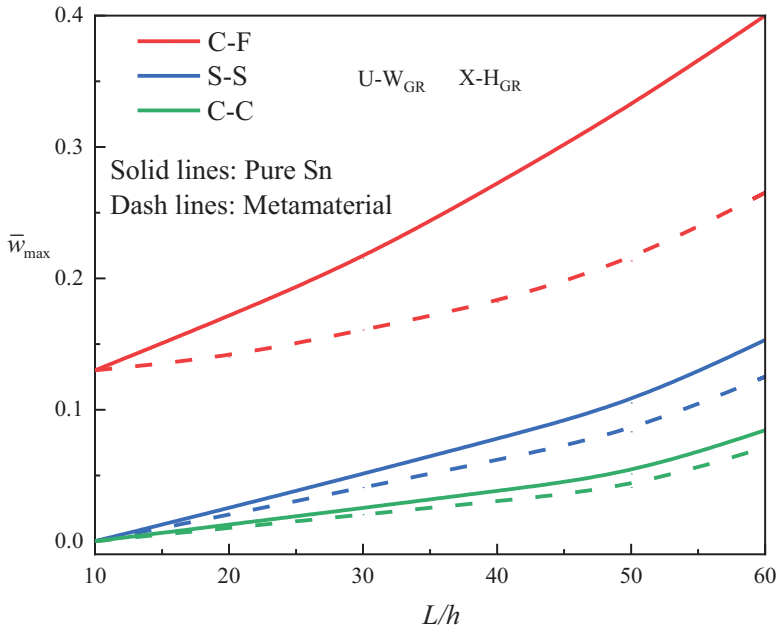


**Figure 8:** Effect of slenderness ratio on the dimensionless maximum deflection of the metamaterial beams and homogeneous beam with three boundaries ($W_{Gr}$ = 2.5 wt%, $H_{Gr}$ = 50%).

It is worth noting that the PINN approximation method adopted in this study is suitable for beams with various boundary and load conditions, although it is not described in detail here for brevity. Among the three boundary conditions (C-C, C-F, S-S), the deflection of the C-F beam was the largest and that of the C-C beam was the smallest. Because the clamped constraint is much stiffer than the S-S and C-F constraints. The addition of graphene origami affected the mechanical behavior of the composite beams. Our results demonstrate that the proposed GOri/Sn metamaterial beam exhibits enhanced bending performance in comparison with a pure metal beam.

## 5 Conclusions

Inspired by deep learning technology, we propose a physically constrained deep learning method to solve the bending problem of graphene origami-reinforced composite microbeams. Bending control equations and boundary conditions are embedded into the loss function of the network as physical information constraints, which can reflect the complex mechanical behavior and ensure the physical rationality of the identification results.

Through an example of composite microbeam bending under a uniformly distributed load, the accuracy of PINNs and traditional analytical solution methods in the calculation results is compared. In addition, a

numerical example of the influence of the graphene origami content and the folding degree of the composite beam on the bending behavior under the size effect verifies the possibility of using a small amount of training data to accurately predict the mechanical behavior in different calculation domains in PINNs. It is worth noting that PINNs are still a promising research field in calculation methods and are excellent candidates for solving inverse and other mechanical problems. For the inverse problem, the traditional forward finite element method is difficult to deal with and usually requires additional optimization algorithms, such as the genetic algorithm and the gradient descent method. In the future, we plan to conduct related research on inverse problems.

**Acknowledgement:** Not applicable.

**Funding Statement:** This work was supported by the Natural Science Foundation of Henan (252300420935), Young Backbone Teacher Training Program of Zhengzhou Normal University (QNGG-232300), Zhengzhou Normal University Undergraduate Innovation and Entrepreneurship Training Program Project (DCY2024011), and Scientific Research Starting Foundation of Zhengzhou Normal University (2021-702442).

**Author Contributions:** Zuoquan Zhu: writing—review and editing, Writing—original draft, visualization, project administration, funding acquisition. Menghan Wang: formal analysis and data curation. Xinyu Li: validation, formal analysis and data curation. Mengxin Zhao: validation, formal analysis. All authors reviewed and approved the final version of the manuscript.

**Availability of Data and Materials:** Data will be made available on request.

**Ethics Approval:** Not applicable.

**Conflicts of Interest:** The authors declare no conflicts of interest.

**Supplementary Materials:** The supplementary material is available online at https://www.techscience.com/doi/10.32604/cmc.2026.076418/s1.

## References

1. Ruocco E, Reddy JN. A closed-form solution for accurate stress analysis of functionally graded Reddy beams. Compos Struct. 2023;307(5):116676. doi:10.1016/j.compstruct.2023.116676.
2. Kim J, Žur KK, Reddy JN. Bending, free vibration, and buckling of modified couples stress-based functionally graded porous micro-plates. Compos Struct. 2019;209(12):879–88. doi:10.1016/j.compstruct.2018.11.023.
3. Shen H-S, Xiang Y, Reddy JN. Effect of negative poisson's ratio on the post-buckling behavior of FG-GRMMC laminated plates in thermal environments. Compos Struct. 2020;253(3):112731. doi:10.1016/j.compstruct.2020.112731.
4. Lu L, Wang S, Li M, Guo X. Free vibration and dynamic stability of functionally graded composite microtubes reinforced with graphene platelets. Compos Struct. 2021;272(12):114231. doi:10.1016/j.compstruct.2021.114231.
5. Zhao S, Zhang Y, Zhang Y, Yang J, Kitipornchai S. Graphene origami-enabled auxetic metallic metamaterials: an atomistic insight. Int J Mech Sci. 2021;212:106814. doi:10.1016/j.ijmecsci.2021.106814.
6. Zhao S, Zhang Y, Zhang Y, Zhang W, Yang J, Kitipornchai S. Genetic programming-assisted micromechanical models of graphene origami-enabled metal metamaterials. Acta Mater. 2022;228:117791. doi:10.1016/j.actamat.2022.117791.
7. Zhao S, Zhang Y, Wu H, Zhang Y, Yang J, Kitipornchai S. Tunable nonlinear bending behaviors of functionally graded graphene origami enabled auxetic metamaterial beams. Compos Struct. 2022;301(9):116222. doi:10.1016/j.compstruct.2022.116222.

8. Zhao S, Zhang Y, Wu H, Zhang Y, Yang J. Functionally graded graphene origami-enabled auxetic metamaterial beams with tunable buckling and postbuckling resistance. Eng Struct. 2022;268(37):114763. doi:10.1016/j.engstruct.2022.114763.
9. Karami B, Ghayesh MH. Dynamics of graphene origami-enabled auxetic metamaterial beams via various shear deformation theories. Int J Eng Sci. 2024;203:104123. doi:10.1016/j.ijengsci.2024.104123.
10. Ezzati H, Pashalou S, Rastgoo A, Ebrahimi F. Vibration analysis of multilayer graphene origami-enabled metamaterial plates. Acta Mech. 2024;235(12):7623–40. doi:10.1007/s00707-024-04117-4.
11. Ebrahimi F, Ahari MF. Vibration control of graphene-origami-enabled meta-material beams with magnetostrictive coatings under temperature gradient. Acta Mech. 2024;235(4):2193–209. doi:10.1007/s00707-023-03823-9.
12. Ebrahimi F, Parsi M. Wave propagation analysis of functionally graded graphene origami-enabled auxetic metamaterial beams resting on an elastic foundation. Acta Mech. 2023;234:6169–90. doi:10.1007/s00707-023-03705-0.
13. Lv Y, Zhang J, Wu J, Li L. Mechanical and thermal postbuckling of functionally graded graphene origami-enabled auxetic metamaterials plates. Eng Struct. 2024;298(1–2):117043. doi:10.1016/j.engstruct.2023.117043.
14. Lei J, He Y, Guo S, Li Z, Liu D. Size-dependent vibration of nickel cantilever microbeams: experiment and gradient elasticity. AIP Adv. 2016;6(10):105202. doi:10.1063/1.4964660.
15. Fleck NA, Muller GM, Ashby MF, Hutchinson JW. Strain gradient plasticity: theory and experiment. Acta Metallurgica Mater. 1994;42(2):475–87. doi:10.1016/0956-7151(94)90502-9.
16. Choi J-H, Kim H, Kim J-Y, Lim K-H, Lee B-C, Sim G-D. Micro-cantilever bending tests for understanding size effect in gradient elasticity. Mater Des. 2022;214(12):110398. doi:10.1016/j.matdes.2022.110398.
17. She G-L, Yuan F-G, Ren Y-R, Xiao W-S. On buckling and postbuckling behavior of nanotubes. Int J Eng Sci. 2017;121(1):130–42. doi:10.1016/j.ijengsci.2017.09.005.
18. Barretta R, Fabbrocino F, Luciano R, Sciarra FMD. Closed-form solutions in stress-driven two-phase integral elasticity for bending of functionally graded nano-beams. Physica E Low Dimens Syst Nanostruct. 2018;97:13–30. doi:10.1016/j.physe.2017.09.026.
19. Zhang P, Qing H. A bi-Helmholtz type of two-phase nonlocal integral model for buckling of Bernoulli-Euler beams under non-uniform temperature. J Therm Stresses. 2021;44:1053–67. doi:10.1080/01495739.2021.1955060.
20. Reddy JN. Nonlocal theories for bending, buckling and vibration of beams. Int J Eng Sci. 2007;45:288–307. doi:10.1016/j.ijengsci.2007.04.004.
21. Brunton SL, Kutz JN. Methods for data-driven multiscale model discovery for materials. J Phys Mater. 2019;2(4):044002. doi:10.1088/2515-7639/ab291e.
22. Bai J, Rabczuk T, Gupta A, Alzubaidi L, Gu Y. A physics-informed neural network technique based on a modified loss function for computational 2D and 3D solid mechanics. Comput Mech. 2023;71(3):543–62. doi:10.1007/s00466-022-02252-0.
23. Tracey BD, Duraisamy K, Alonso JJ. A machine learning strategy to assist turbulence model development. In: 53rd AIAA Aerospace Sciences Meeting; 2015 Jan 5–9; Kissimmee, FL, USA.
24. Yuan L, Ni Y-Q, Deng X-Y, Hao S. A-PINN: auxiliary physics informed neural networks for forward and inverse problems of nonlinear integro-differential equations. J Comput Phys. 2022;462:2022–111260. doi:10.1016/j.jcp.2022.111260.
25. Raissi M, Perdikaris P, Karniadakis GE. Physics-informed neural networks: a deep learning framework for solving forward and inverse problems involving nonlinear partial differential equations. J Comput Phys. 2019;378:686–707. doi:10.1016/j.jcp.2018.10.045.
26. Jin X, Cai S, Li H, Karniadakis GE. NSFnets (Navier-Stokes flow nets): physics-informed neural networks for the incompressible Navier-Stokes equations. J Comput Phys. 2021;426:109951. doi:10.1016/j.jcp.2020.109951.
27. Li W, Fang R, Jiao J, Vassilakis GN, Zhu J. Tutorials: physics-informed machine learning methods of computing 1D phase-field models. APL Mach Learn. 2024;2(3):031101. doi:10.1063/5.0205159.
28. Cai S, Wang Z, Wang S, Perdikaris P, Karniadakis GE. Physics-informed neural networks for heat transfer problems. J Heat Transf. 2021;143(6):060801. doi:10.1115/1.4050542.

29. Xue Y, Li Y, Zhang K, Yang F. A physics-inspired neural network to solve partial differential equations—application in diffusion-induced stress. Phys Chem Chem Phys. 2022;24(13):7937–49. doi:10.1039/D1CP04893G.
30. Fallah A, Aghdam MM. Physics-informed neural network for bending and free vibration analysis of three-dimensional functionally graded porous beam resting on elastic foundation. Eng Comput. 2024;40(1):437–54. doi:10.1007/s00366-023-01799-7.
31. Kianian O, Sarrami S, Movahedian B, Azhari M. PINN-based forward and inverse bending analysis of nanobeams on a three-parameter nonlinear elastic foundation including hardening and softening effect using nonlocal elasticity theory. Eng Comput. 2024;41(1):71–97. doi:10.1007/s00366-024-01985-1.
32. Bazmara M, Mianroodi M, Silani M. Application of physics-informed neural networks for nonlinear buckling analysis of beams. Acta Mech Sin. 2023;39(6):422438. doi:10.1007/s10409-023-22438-x.
33. Shi P, Wang Z, Hoang VNV, Zhao W, Xie H, Kiran R, et al. Analytical and neural network-based approaches for mechanical postbuckling analysis of simply-supported functionally graded graphene origami-enabled auxetic metamaterial plates. Thin-Walled Struct. 2025;216:113606. doi:10.1016/j.tws.2025.113606.
34. Mirsabetnazar A, Ansari R, Ershadi Zargar M, Rouhi H. Annular sector plates made of FG graphene origami-enabled auxetic metamaterial under bending and buckling loading: a VDQ-based approach. Mater Today Commun. 2024;41:110629. doi:10.1016/j.mtcomm.2024.110629.
35. Mirsabetnazar A, Ansari R, Ershadi Zargar M, Rouhi H. Bending, buckling and free vibration analysis of functionally graded graphene origami-enabled auxetic metamaterial beams based on the VDQ method. J Braz Soc Mech Sci Eng. 2024;46(12):726. doi:10.1007/s40430-024-05298-8.
36. Mirsabetnazar A, Ansari R, Ershadi MZ, Rouhi H. Tunable bending and buckling behaviors of circular plates made of FG graphene origami-enabled auxetic metamaterials. Int J Struct Stab Dyn. 2024;25(16):2550168. doi:10.1142/S0219455425501688.
37. Yang F, Chong ACM, Lam DCC, Tong P. Couple stress based strain gradient theory for elasticity. Int J Solids Struct. 2002;39(10):2731–43. doi:10.1016/S0020-7683(02)00152-X.
38. Jena SK, Chakraverty S, Mahesh V, Harursampath D. Application of Haar wavelet discretization and differential quadrature methods for free vibration of functionally graded micro-beam with porosity using modified couple stress theory. Eng Anal Bound Elem. 2022;140(8):167–85. doi:10.1016/j.enganabound.2022.04.009.
39. Schmidhuber J. Deep learning in neural networks: an overview. Neural Netw. 2015;61(3):85–117. doi:10.1016/j.neunet.2014.09.003.
40. Li W, Bazant MZ, Zhu J. A physics-guided neural network framework for elastic plates: comparison of governing equations-based and energy-based approaches. Comput Methods Appl Mech Eng. 2021;383(34):113933. doi:10.1016/j.cma.2021.113933.
41. Guo H, Zhuang X, Rabczuk T. A deep collocation method for the bending analysis of kirchhoff plate. Comput Mater Contin. 2019;59(2):433–56. doi:10.32604/cmc.2019.06660.
42. Rumelhart DE, Hinton GE, Williams RJ. Learning representations by back-propagating errors. Nature. 1986;323:533–6. doi:10.1038/323533a0.
43. Janocha K, Czarnecki WM. On loss functions for deep neural networks in classification. arXiv:1702.05659. 2017.
44. Baydin AG, Pearlmutter BA, Radul AA, Siskind JM. Automatic differentiation in machine learning: a survey. J Mach Learn Res. 2018;18:1–43.
45. Kingma DP, Ba J. Adam: a method for stochastic optimization. arXiv:1412.6980. 2014.
46. Nwankpa C, Ijomah WL, Gachagan A, Marshall S. Activation functions: comparison of trends in practice and research for deep learning. arXiv:1811.03378. 2018.
47. Qi Y, Hector LGJ, James C, Kim KJ. Lithium concentration dependent elastic properties of battery electrode materials from first principles calculations. J Electrochem Soc. 2014;161(11):F3010–8. doi:10.1149/2.0031411jes.
48. Park SK, Gao X-L. Bernoulli–Euler beam model based on a modified couple stress theory. J Micromech Microeng. 2006;16(11):2355–9. doi:10.1088/0960-1317/16/11/015.

49. Ezzati H, Rastgoo A, Ebrahimi F. Thermal buckling analysis of functionally graded graphene origami-enabled auxetic metamaterial beams rested on an elastic foundation. Structures. 2024;70(9):107764. doi:10.1016/j.istruc.2024.107764.
50. Zhang C, Lu C, Pei L, Li J, Wang R, Tieu K. The negative poisson's ratio and strengthening mechanism of nanolayered graphene/Cu composites. Carbon. 2019;143(5887):125–37. doi:10.1016/j.carbon.2018.10.097.